Aging Mechanism For Calendar Aging of Li-Ion Cells With Si/Graphite Anodes

Journal of The Electrochemical Society, 2024 **171** 010510

Aging Mechanism For Calendar Aging of Li-Ion Cells With Si/Graphite Anodes

Katharina Bischof,[1] Marius Flügel,[1] Markus Hölzle,[1] Margret Wohlfahrt-Mehrens,[1,2] and Thomas Waldmann[1,2,z]

[1]*ZSW—Zentrum für Sonnenenergie- und Wasserstoff-Forschung Baden-Württemberg, Helmholtzstrasse 8, D-89081 Ulm, Germany*
[2]*HIU—Helmholtz Institute Ulm for Electrochemical Energy Storage, Helmholtzstraße 11, D-89081 Ulm, Germany*

Calendar aging of Li-ion batteries with Si/graphite electrodes was investigated within this study. A total of 121 single-layer pouch full cells with either graphite or Si/graphite (3.0 wt−%, 5.8 wt−% and 20.8 wt−% Si) anodes and NMC622 cathodes with the same N/P ratio were built on pilot-scale. Calendar aging was studied at SoC 30%, 60%, and 100%, as well as temperature (25 °C, 45 °C, 60 °C) and time dependence. The aging data was analyzed in terms of capacity fade and a square-root behavior was observed. Differential voltage analysis (DVA) has been performed as a function of aging time. The observed temperature and time dependence is best described by time dependent, 3D Arrhenius plots. Post-Mortem analysis (SEM, EDX, GD-OES) is applied to investigate the changes on electrode and material level. Conclusions are drawn on the main aging mechanisms for calendar aging of Li-ion cells with Si/graphite anodes and differences between Si/graphite and pure graphite anodes are discussed. The Si-containing cells show a combination of lithium inventory loss and a loss of accessible Si active material, both caused by SEI growth.
 [DOI: 10.1149/1945-7111/ad1b7c]

Manuscript submitted August 11, 2023; revised manuscript received December 14, 2023. Published January 16, 2024.

Supplementary material for this article is available online

An adequate lifetime of the Li-ion batteries (LIBs) is critical to ensure market acceptance of such batteries in portable, mobile and stationary applications.[1] In addition, high energy density is another important factor that determines the competitiveness of LIBs. Especially for electric vehicles, further increase in battery energy density is of great interest to achieve longer driving ranges in combination with smaller batteries.[2,3] Silicon (Si) is considered as the most promising anode material that, due to its high theoretical capacity of 3,579 mAh g^{-1} at room temperature,[4] would enable a significant increase in both gravimetric and volumetric energy density as well as reducing raw materials costs.[2,5,6] However, the alloying reaction of Si with Li^+-ions leads to a large volume expansion of the anode, typically resulting in poor cycling stability and rapid capacity loss of pure Si electrodes.[2,6,7] As a consequence, neither pure graphite nor pure Si anodes can meet the stringent requirements of future electrical devices. Therefore, silicon/graphite composite (Si/graphite) anodes with up to 4 wt−% of Si[8] are currently used in commercially available state-of-the-art LIBs to improve both the capacity without suffering in cycle life of such batteries.[2,9]

Cycling aging of Li-ion cells with graphite and Si/graphite anodes was investigated in detail over the last years. Different groups have identified either loss of anode active material (LAAM)[8,10–12] or loss of Li inventory (LLI)[8,13–15] as the main root causes of capacity loss. LLI is caused by Li reacting irreversibly and forming SEI which can take place on both graphite[16,17] and Si/graphite anodes.[11] LAAM can occur for both graphite and Si particles by electronic isolation of particles e.g., resulting from electrode cracks. However, only Si particles can show particle fracture due to volume expansion[18] and SEI growth[8,11] which results in additional LAAM. We have recently shown for three types of commercial cells, that LAAM occurs only for certain types of Si components.[8]

As recently pointed out by McBrayer et al., there is a lack of understanding on the mechanisms of calendar aging in case of Si/graphite anodes,[5] since only few studies exist on this topic.[15,19–21] Zilberman et al. investigated calendar aging of commercial cylindrical cells (~3.5 wt−% Si).[19] The authors concluded that for the cell type investigated, LAAM regarding the Si component was the main cause of capacity fade.[19]

Therefore, we systematically investigated calendar aging of cells with Si/graphite anodes in comparison to pure graphite anodes, with the aim of a comprehensive picture for the trends regarding time, temperature, SoC, and Si content. For this purpose, 121 pouch cells were built and calendar aged at different storage conditions. The aging behavior is investigated in terms of capacity fade. Differential voltage analysis (DVA) on cell level is added to this investigation to gain further insight into electrode processes. The rate dependence of the capacity fade over time and temperature is best described by three-dimensional (3D) Arrhenius plots. Investigations on electrode and material level are performed by Post-Mortem analysis using SEM/EDX and glow discharge optical emission spectroscopy (GD-OES). Finally, we draw conclusions on the main aging mechanisms for calendar aging of Li-ion cells with Si/graphite anodes and thereby discuss differences between Si/graphite and pure graphite anodes.

Experimental

Electrode manufacturing.—Graphite active material and three Si/graphite composite active materials with different Si contents were purchased from Iopsilion (China). The Si contents in the anode electrodes were 0 wt−% (Graphite), 3.0 wt−% (SiG3.0), 5.8 wt−% (SiG5.8) and 20.8 wt−% (SiG20.8). Anode coatings were prepared using active material, CMC binder (TIMCAL, Switzerland), SBR binder (ZEON, Japan), and SuperC65 conductive additive (Nippon paper Industries, Japan) with weight ratios of 94:2:2:2 (Graphite, SiG3.0 and SiG5.8) and 90:3:3:4 (SiG20.8). Cathode coatings are prepared by coating N-methyl pyrrolidone (NMP) based slurries with 94 wt−% NCM622 active material (BASF, Germany), 2 wt−% PVDF (Solvay, Belgium), 2 wt−% carbon black (TIMCAL, Switzerland), and 2 wt−% graphite (TIMCAL, Switzerland) onto Al foil. The cathodes were calendered at 100 °C roll temperature to a density of 3.2 g cm^{-3}. Both, anodes and cathodes were produced on ZSW's pilot coating lines. These electrodes are from the same production batch as in our previous study by Flügel et al.[8,22] More details on the electrode production and their properties (density, porosity, tortuosity) can be found there.[8,22]

Cell manufacturing.—In total 121 single-layer pouch full cells were assembled at ZSW's pilot line with the four negative electrodes

[z]E-mail: thomas.waldmann@zsw-bw.de

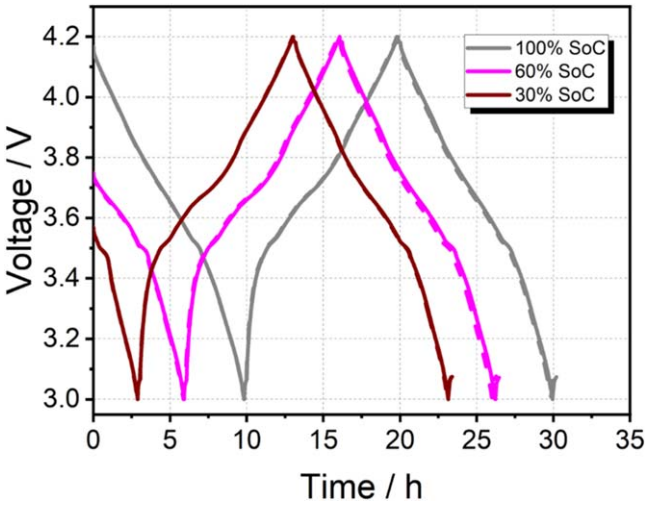

Figure 1. Exemplary representation of the time course of a check-up routine for all three SoCs examined. The dashed lines correspond to the reproduction of the voltage curve by a second cell aged under the same conditions (SiG5.8, 25 °C). The discharge capacity of the full cycle was used to determine the irreversible capacity loss caused by calendar aging.

and complementary NMC622 cathodes described above. The areal capacity of the cathodes is matched to the areal capacity of the respective anode in such a way that irreversible active material losses due to the Si component are compensated. As a result, a similar N/P ratio of 1.1 is achieved for all cell types.[8,22]

The pouch full cells were assembled using one single-sided coated anode with an area of 26 cm^2 and one single-sided coated cathode with an area of 24 cm^2, Celgard 2325 separator. Graphite pouch cells were typically filled with 900 μl of VC containing electrolyte (1.0 M $LiPF_6$ in EC:DEC (3:7 wt−%) + 2 wt−% VC) and Si pouch cells were filled with 900 μl of FEC containing electrolyte (1.0 M $LiPF_6$ in EC:DEC (3:7 wt−%) + 10 wt−% FEC). To exclude any effect of the electrolyte additive on the capacity fade behavior, 13 graphite cells were additionally filled with the FEC containing electrolyte. VC was chosen as the primary electrolyte additive for the graphite cells as it is considered to be the most effective additive to ensure a long lifetime of graphite cells.[23,24] Unless otherwise stated, graphite cells in the following always refer to these graphite cells with VC. As FEC is reported to form a more stable and flexible SEI on Si,[25,26] it was used as the electrolyte additive for the Si-containing cells.

Calendar aging procedure.—All electrochemical tests were conducted at ZSW with a MACCOR 4200 system at room temperature. Formation was performed after a rest period of 12 h with three cycles at 0.1 C in the voltage range from 2.8 V to 4.2 V. CC-CV (constant current - constant voltage) mode (CV until I < 0.05 C) was used for charging and CC mode for discharging.

To investigate calendar aging, the cells were charged to three different SoCs (100%, 60%, and 30%) at 0.1 C after formation and aged at three different temperatures (25 °C, 45 °C, and 60 °C). A SoC of 30% and 60% was achieved by first discharging the corresponding cells to a lower voltage limit of 3.0 V in a CC discharge step and then charging them for 3 h and 6 h, respectively, using CC mode. The cells with a target SoC of 100% were charged to 4.2 V using CC-CV mode without prior discharge. Subsequently, the cells were stored in climate chambers (Vötsch) at 25 °C and 45 °C and in a home-made thermobox at 60 °C. For the graphite-containing cells with FEC as electrolyte additive only the combinations of the aging parameters 60% SoC or 100% SoC and 45 °C or 60 °C were tested. In this case, the cells were placed in two different climate chambers (45 °C: Binder, 60 °C: CTS) than all other cells investigated. At least two cells with the same parameters were built for each of the three influencing factors: Si content, SoC, and temperature. If a deviating electrochemical behavior occurred between two cells of the same type, further cells were calendar aged under the same conditions.

The progress of calendar aging was monitored by regular electrochemical check-ups. For the cells stored at 25 °C and 45 °C, these took place approximately every four weeks. Since the fastest aging was expected at a temperature of 60 °C, check-ups for these cells were performed at bi-weekly intervals. For this purpose, cells aged at 45 °C and 60 °C were first cooled to room temperature for ~1 h. The check-up routines (Fig. 1) then included a CC discharge step until a lower voltage limit of 3.0 V was reached, followed by a CC-CV charge and CC discharge cycle in the voltage range of 3.0 V to 4.2 V. To prevent the initiation of potential side reactions caused by the check-ups, a low C-rate of 0.1 C was used for all charge and discharge processes. Finally, the cells were charged to their original SoCs using the same protocols described above. The 0.1 C used for charging was always based on the discharge capacity from the full cycle of the most recent check-up. This means that this capacity was adjusted for each check-up routine to match the required SoCs to the current aging state of the cells.

To determine the current SoH of the cells at time t, the discharge capacity Q(t) from the full cycle of each check-up was referenced to the discharge capacity Q(t = 0) of the third formation cycle to 3.0 V according to equation

$$SoH\,(t) = \frac{Q(t)}{Q(t=0)} \qquad [1]$$

After reaching SoH = 80%, which was defined as end-of-life (EoL) criterion, the aging was stopped.

Determination of aging rates.—To determine the aging rates, the SoHs of the cells were plotted versus time t. All time periods in which the cells were in check-ups were subtracted in order to consider only the real duration of the calendar aging. The capacity decrease curves were then fitted in Origin using the relationship

$$SoH = 100 + a\sqrt{t} \qquad [2]$$

with the parameter a and the intercept SoH(t = 0) = 100%. The corresponding aging rates r were determined from the time derivative

$$r = -\frac{dSoH}{dt} = -\frac{a}{2\sqrt{t}} \qquad [3]$$

For graphite-containing cells aged at a temperature of 25 °C, an increase in SoH was initially observed. To determine their aging rates analogously to the described procedure, the maximum SoH reached during aging was normalized to SoH(t = 0) = 100% in each case.

Post-mortem characterization.—SEM top view images of the anodes were measured at an accelerating voltage of 5 kV using a JSM-IT500 microscope (JEOL) equipped with a tungsten filament. EDX was performed at an accelerating voltage of 20 kV. A LEO 1530 VP microscope (Zeiss) equipped with a Gemini field emission column was used to characterize anodic cross-sections. Measurements were recorded at an accelerating voltage of 5 kV using a SE detector. Electrode cross-sections were prepared with a Hitachi IM4000Plus broad-beam argon ion milling system, using an ion beam voltage of 5 kV. During sample preparation for SEM (top view and cross-section), the samples were exposed to air.

GD-OES depth profiling analysis was performed with a GDA750 measurement device (Spectruma, Germany). Measurements were carried out in radio frequency (RF) mode at a frequency of 2501 Hz, at a discharge voltage of 550 V and a pressure of 2 hPa. The sputtering gas was a mixture of 1% H_2 in Ar (both 6.0 purity). The specific emission line of 670.7 nm was used for the detection of Li.

Results and Discussion

Capacity fade during calendar aging.—Figure 2 shows the capacity decay during calendar aging at different temperatures vs time for 100% SoC. It is noted that the scattering of data of reproduced cells is comparable to commercial cells described by others.[27]

The capacity decrease in Fig. 2 is characterized by a strong temperature dependence, which is reflected in an increasing aging with increasing temperature. The cells aged at a temperature of 25 °C still exhibit a SoH $>$ 80% after more than 200 d regardless of the Si content (blue data points in Fig. 2), while the cells at a storage temperature of 60 °C have already reached their EoL criterion (SoH $=$ 80%) by this time (red data points in Fig. 2). Between the cells aged at 60 °C, a capacity loss increasing with increasing Si content can also be observed (red data points in Fig. 2). While the graphite based cells with VC as electrolyte additive (Fig. 2a) reached SoH $<$ 80% only after more than 150 d (10 check-ups), the Si-containing cells with SiG3.0, SiG5.8 and, SiG20.8 anodes fell below the EoL criterion already after 59–91 days (4–6 check-ups), about 60 d (4 check-ups) and 40–52 d (2–3 check-ups), respectively. A similar trend can be observed for the other temperatures, but still the differences between the Si contents are the strongest at 60 °C aging. Compared to the pure graphite based cells (regardless of the electrolyte additive used), the capacity of the Si/graphite cells always decreases faster. This trend is similar to the deteriorated calendar lifetime of Si-containing LIBs compared to their pure graphite counterparts described by McBrayer et al. due to the presence of Si.[5]

Similar trends were also found for the SoCs of 60% and 30% (see Figs. S1 and S2). Only the SiG5.8 cells stored at 30% SoC appear to age at a similar rate within the scattering at 45 °C as at 60 °C. This finding is reproducible for two cells (see yellow data points which are bleached out in Fig. S2c). However, there was an extremely high internal resistance of $>$1000 mΩ measured before performing the check-ups of these two cells, possibly leading to the fast capacity decrease. In perspective to the overall data set, this behavior therefore seems to be an outlier. Overall, the capacity losses are smaller for the lower SoCs compared to 100% SoC, with only minor differences between 60% and 30% SoC (see Figs. S3, S4, and S5).

At 100% SoC the graphite cells with FEC as electrolyte additive show a similar capacity decay at 45 °C as well as at 60 °C compared to their VC containing counterparts (see Fig. 2a). In this case, the capacity fade curves seem to be little affected by the different additives. In contrast, at 60% SoC (see Fig. S1a) the capacity losses after around 50 d are smaller for the graphite cells with FEC

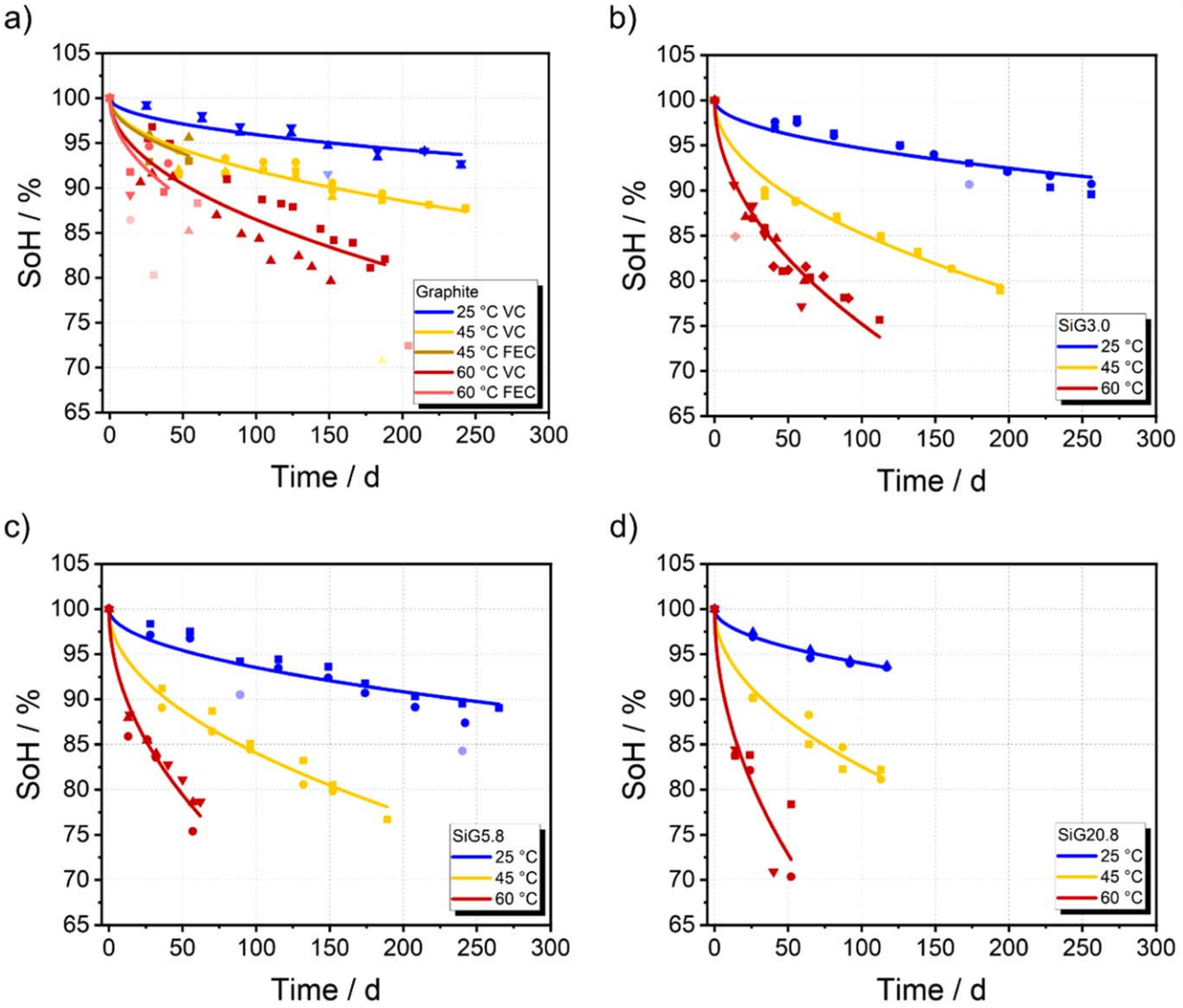

Figure 2. Capacity degradation for (a) graphite, (b) SiG3.0, (c) SiG5.8, and (d) SiG20.8 based cells at a storage SoC of 100% over calendar aging time. The points correspond to the measured data and the lines to the fitting results obtained with Eq. 2. The bleached data points represent outliers and were not included in the fits.

Table I. Summary of fit results with Eq. 2 for capacity decrease of cells aged at SoC of 100%.

Anode	Temperature	Fit parameter a	R^2
Graphite	25 °C	−0.41 ± 0.02	0.88
	45 °C	−0.81 ± 0.02	0.91
	60 °C	−1.35 ± 0.05	0.83
SiG3.0	25 °C	−0.53 ± 0.02	0.90
	45 °C	−1.48 ± 0.02	0.99
	60 °C	−2.48 ± 0.05	0.97
SiG5.8	25 °C	−0.65 ± 0.03	0.90
	45 °C	−1.59 ± 0.03	0.98
	60 °C	−2.91 ± 0.07	0.97
SiG20.8	25 °C	−0.60 ± 0.01	0.99
	45 °C	−1.74 ± 0.05	0.97
	60 °C	−3.84 ± 0.19	0.93

compared to the graphite cells with VC at both temperatures. This indicates an even slower aging of the graphite cells when using FEC as electrolyte additive in comparison with the Si-containing cells.

The shape of the capacity fading curves is very similar for all Si contents, temperatures, and SoCs and is characterized by a reduced slope over aging time. In order to mathematically describe the time dependence of the capacity degradation, the square-root function shown in Eq. 2 was used to describe the whole data set with only the parameter a. A similar approach was used in several empirical calendar aging models developed by other authors for cells with pure graphite anodes.[27–30] Individual data points that obviously do not follow the general trend were declared as outliers and not included in the fits.

As shown in Table I, the quality of the fitting curves at 100% SoC is in a good correlation with the experimental data with R^2 values mostly being ⩾0.90. Only the fit for the graphite based cells stored at 60 °C shows a slightly lower R^2 value (⩾0.83) due to strong scattering of the data points. Equation 2 also provides good fit results for the SoCs of 60% and 30%, with R^2 values (with one exception) of R^2 ⩾0.85 (see Tables S1 and S2).

In the literature, a square-root dependence of the capacity decrease over time is often attributed to the formation of an insulating SEI layer with gradually slower growth over time.[27,28,31–33] The cause of the continuously decreasing growth rate of SEI is thereby discussed via different approaches.[34] These include transportation mechanisms such as solvent diffusion,[32,35] electrical conductivity,[31,36] or diffusion of neutral Li-interstitials[37,38] through the SEI, which all conclude a $\sqrt{t}$-dependence for the long-term capacity fade.[34] The good agreement of the experimental data with the square-root function in Eq. 2, gives a hint that SEI growth may also be present in cells with Si/graphite anodes. Since this is associated with reductive decomposition of $LiPF_6$ from the electrolyte, LLI can be expected.[17,39,40]

Analysis of time and temperature dependence via 3D Arrhenius plots.—In order to investigate the influence of temperature on the rate of capacity degradation in more detail, the Arrhenius equation was applied

$$r = A \exp\left(-\frac{E_a}{k_B T}\right) \quad [4]$$

with A as the pre-exponential factor, the activation energy E_a, the Boltzmann constant k_B, and the absolute temperature T.

From the square-root function in Eq. 2, a continuous function for the aging rate (Eq. 3) can easily be derived analytically. For the Arrhenius plot, the aging rates r were first determined for the different aging conditions according to Eq. 3 using the parameters a resulting from the square-root fits (Eq. 2). Compared to Kucinskis et al.,[41] this procedure allows to simultaneously capture the temporal change of the aging rate. Therefore, Fig. 3 shows the logarithmic aging rates for the different SoCs as a function of both temperature and time in a 3D Arrhenius plot. We note that the Arrhenius-like behavior is not found along the plotted lines, but perpendicular to them for each time point t (see exemplary 2D projections in ln(r) vs $(k_B T)^{-1}$ plain in Fig. 3a).

The 3D Arrhenius plots are characterized by the $\sqrt{t}$-dependence of the capacity loss discussed earlier. For all combinations of temperature and SoC studied, the aging rates for the graphite based cells (black curves in Fig. 3) are lower than for their Si-containing counterparts. Thus, the presence of the Si component appears to have an accelerating effect on the aging rate. This could result from a different composition of the SEI compared to the pure graphite anodes and their different properties.[5,15]

Since all aging rates in Fig. 3 were determined by Eq. 3, their relative temperature dependence for one cell type does not change over time. To focus on the temperature influence in more detail, a 2D section through the 3D plots at t = 1 d was set as an example and the associated aging rates were fitted linearly over the investigated temperature range from 25 °C to 60 °C. The resulting 2D Arrhenius plots for the different SoCs are shown in Figs. 4a–4c.

The results of the linear fits are listed in Table II and are characterized by R^2 values ⩾ 0.97 for all cell types and aging conditions. The high R^2 values indicate that the temperature dependence of the capacity loss rates can be adequately described by the Arrhenius Eq. 4. The linearity shows additionally that there is most likely one dominating aging mechanism at all temperatures studied.[42] A different behavior reported in literature is for example the temperature dependent transition from SEI growth at high temperatures to Li plating at low temperatures under cycling aging conditions, leading to a slope change in the Arrhenius plot.[16,41,43–46] The only exception from the Arrhenius behavior in the present study on calendar aging is the fit for the SiG5.8 cells aged at 30% SoC. However, the deviating correlation coefficient is again caused by the unusually fast capacity loss of the cells aged at 45 °C discussed earlier (see yellow data points in Fig. S2c) and should therefore not be interpreted as a contradiction to the otherwise assumed Arrhenius-like behavior.

In the literature, Arrhenius-like behavior in the temperature range studied is attributed to the growth of the SEI, which was additionally verified by Waldmann et al. through Post-Mortem analyses.[16,47] Thus, the observed validity of the Arrhenius-like relationship between the aging rates and the storage temperature reinforces the hypothesis that the calendar aging results mainly from LLI.

The values of the activation barriers E_a obtained from the slopes of the linear fits from Figs. 4a–4c are plotted against the Si content of the anode in Fig. 4d. At 30% and 60% SoC there is a general decrease of the values of E_a observable with increasing Si content. The opposite trend is evident for 100% SoC. In this case, the value of E_a is lowest for the cell with the graphite anode and highest for the one with the SiG20.8 anode. Since the value of E_a describes the influence of temperature on the aging rate, it can be concluded that for 100% SoC there is a stronger temperature effect on the aging rate with increasing Si content, whereas this effect decreases with higher Si content for the lower SoCs. In this case, the temperature influence on the aging rate is strongest for the graphite cells. However, the observed trends in E_a cannot be interpreted directly regarding the aging mechanism. As these are complex processes, resulting from several different parallel and consecutive reactions,[17] it is not possible to assign the values of E_a shown here to a specific reaction. Rather, E_a should be seen as an overall apparent activation energy for the whole aging process. The exact values of the activation barriers are listed in Table II. The observed E_a values are in the same order of magnitude as found by others[48,49] and by our group.[16,47]

Differential voltage analysis.—DVA allows the differentiation of various aging mechanisms such as LAAM and LLI.[50–52] Since, a

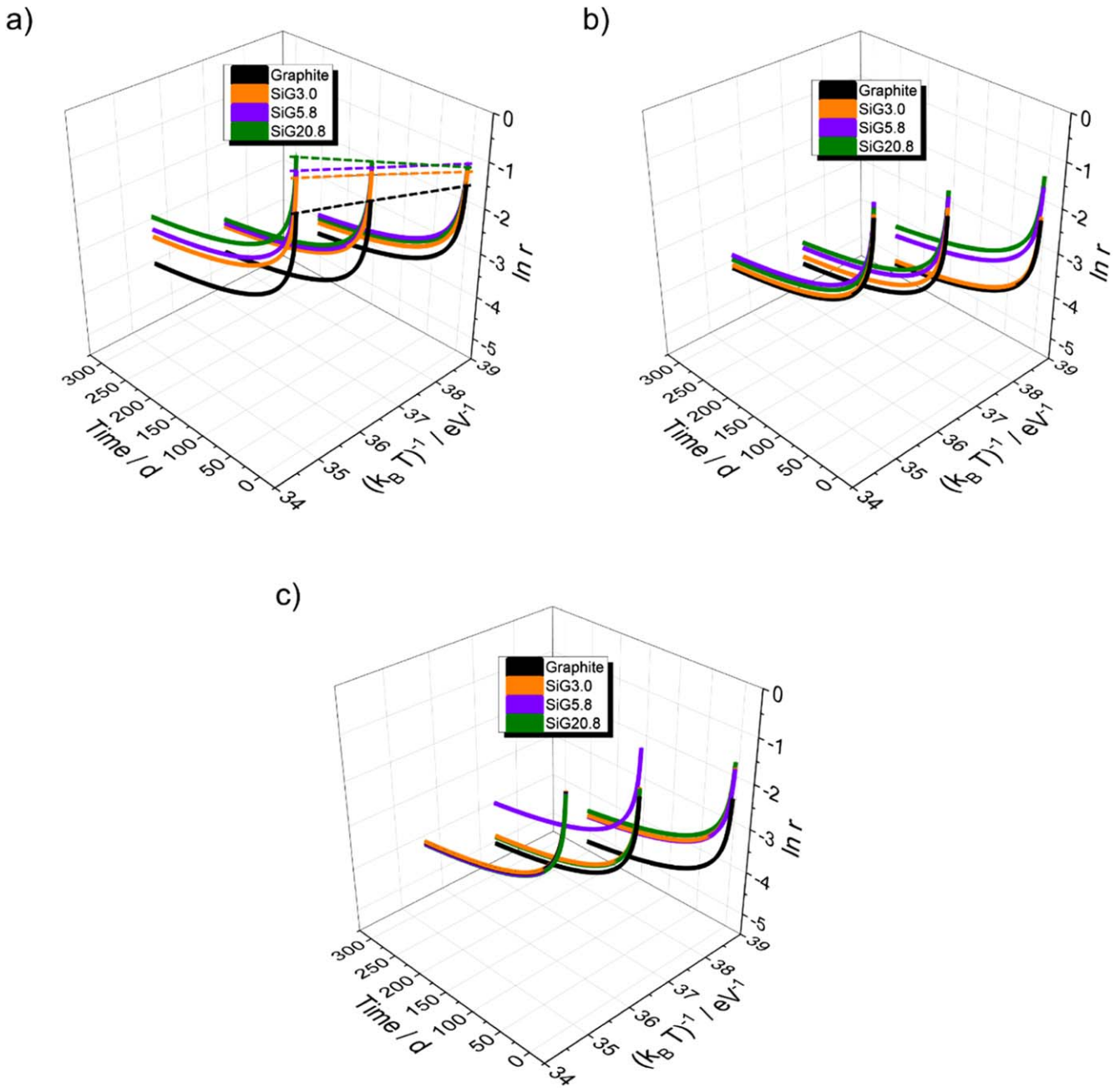

Figure 3. 3D Arrhenius plots for the calendar aging at (a) 100%, (b) 60% and (c) 30% SoC. The aging rates were calculated according to Eq. 3 as a function of time t for the three temperatures studied, 25 °C, 45 °C, and 60 °C. The error bars of the aging rates are so small that they cannot be seen in the plots. The exemplary 2D projections in the ln(r) vs $(k_BT)^{-1}$ plain in a) are cuts through the 3D data and correspond to the representation in Fig. 4a.

similar main aging mechanism can be assumed for all aging conditions, only the discharge curves of the cells aged at 45 °C and a storage SoC of 100% were analyzed here. The corresponding DVA results for one cell of each Si content are shown in Fig. 5. It should be noted that the capacities from all check-ups are normalized to a SoC of 100% for better comparability, i.e. 100% SoC corresponds to the fully charged state, independent from the aging state.

For the graphite based cell (Fig. 5a), two peaks, G_1 and G_2, are obtained in accordance with the literature.[8,50,51] The central graphite peak G_1 is located at a higher SoC than the G_2 peak and corresponds to the transition between the potential plateaus of the LiC_6 and LiC_{12} phases during the delithiation of the graphite anode.[53] In the discharge curves of Si/graphite cells, the presence of the Si component is manifested by a less steep voltage drop in the direction of delithiation due to the higher working potential of Si compared to graphite.[54,55] This results in two additional peaks in the DVAs of SiG3.0, SiG5.8, and SiG20.8 based cells (Figs. 5b–5d) at low SoCs which can be attributed to the Si component.[12,19] In consistence with Flügel et al. these peaks are referred to as S_1 and S_2.[8] With higher Si content, both the graphite and Si peaks are shifted to higher SoCs. As expected, no characteristic cathode peaks were observed for NMC622.[56,57]

With calendar aging, a shift of all identified peaks to higher SoCs is observed for all cell types. The largest change takes place between the formation and the first check-up, which is based on the strongest capacity decrease at the beginning of aging as explained above. The shift of the graphite peak G_1 is clearly more pronounced for the Si-containing cells than for the graphite cells, which indicates stronger aging with increasing Si content. This is consistent with the aging

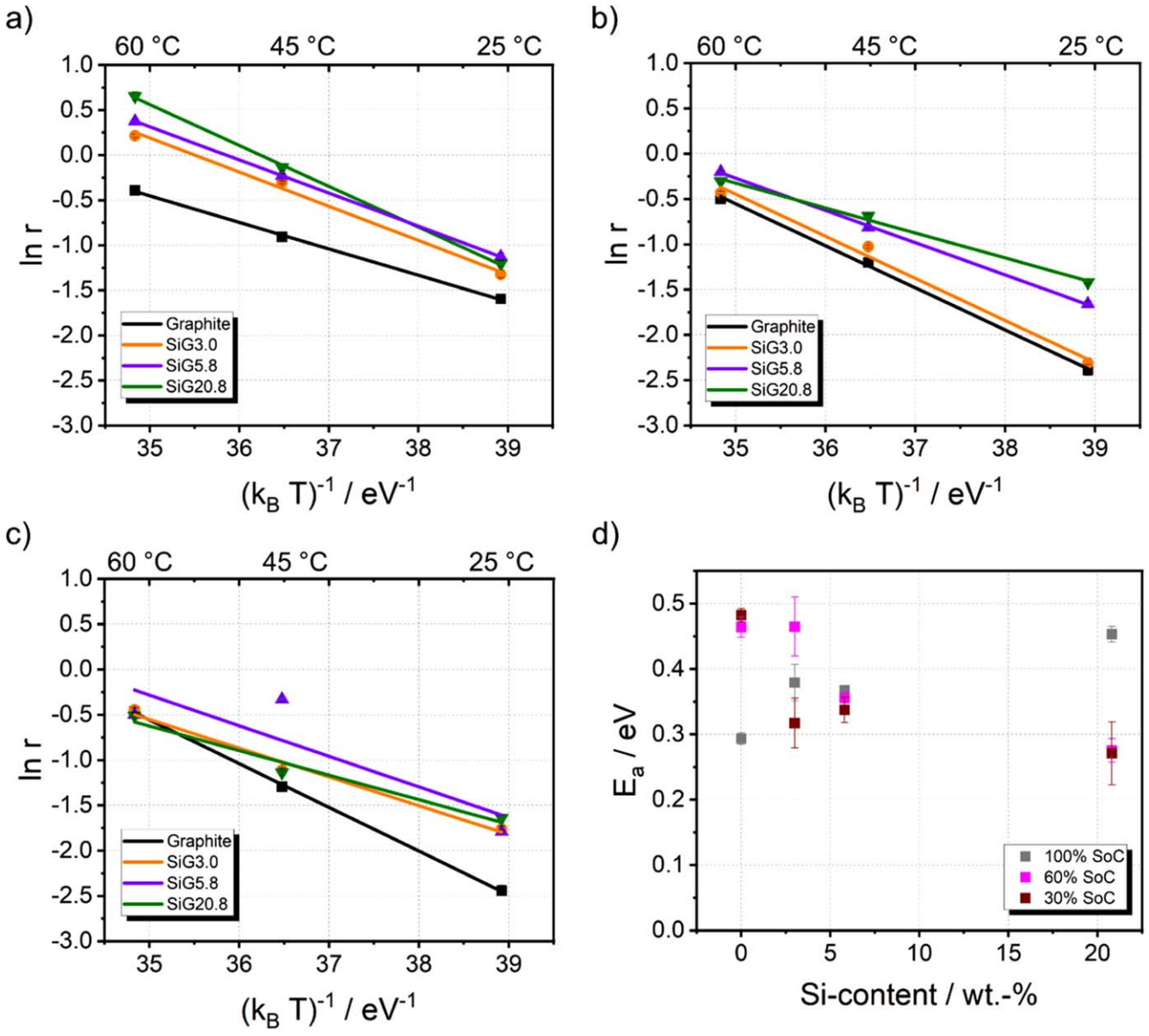

Figure 4. Arrhenius plots for calendar aging at a SoC of (a) 100%, (b) 60%, (c) 30% at the onset of aging. The aging rates were obtained from Fig. 3 by a cross-section at t = 1 d. The error bars are so small that they cannot be seen in this representation. The lines correspond to the linear fits of the aging rates over the temperature range from 25 °C to 60 °C. (d) Plot of the activation energies obtained from the linear fits from (a)–(c) versus the Si content of the cells.

Table II. Summary of fit results with Arrhenius equation (Eq. 4) for temperature dependence of capacity decrease rates.

Anode	SoC	E_a	R^2
Graphite	100%	0.29 ± 0.01 eV	1.00
	60%	0.46 ± 0.02 eV	1.00
	30%	0.48 ± 0.01 eV	1.00
SiG3.0	100%	0.38 ± 0.03 eV	0.99
	60%	0.46 ± 0.05 eV	0.99
	30%	0.32 ± 0.04 eV	0.98
SiG5.8	100%	0.37 ± 0.00 eV	1.00
	60%	0.36 ± 0.01 eV	1.00
	30%	0.34 ± 0.02 eV	0.76
SiG20.8	100%	0.45 ± 0.01 eV	1.00
	60%	0.28 ± 0.02 eV	1.00
	30%	0.27 ± 0.05 eV	0.97

results (see above). The intensity of the Si peaks decreases for all Si contents. Only for S_2 of the SiG20.8 cell no noticeable change in intensity can be observed, however, this peak is already very flat and broad at the beginning in the formation. In addition to the shift in S_1 and S_2, the decrease in intensity of these peaks implies a decrease in the Li storage capability in Si. Accordingly, the higher capacity loss of the SiG3.0, SiG5.8, and SiG20.8 based cells compared to the pure graphite cell could be caused by LAAM, a prominent aging mechanism in the Si-containing cells.[8,11]

For a differentiated consideration of the cause of the capacity decreases and to verify a possible LAAM, the total capacities shown in the DVAs (0% SoC–100% SoC) were each divided into two characteristic capacity fractions Q_1 and Q_2 (Fig. 5) following Keil et al.[50,51] A similar approach to interpret the DVA results for commercial Si/graphite cells was also adopted by Zilberman et al.[19] Here, Q_1 corresponds to the distance between 0% SoC and the G_1 peak and contains information about the storage capacity of the anode.[50,51] A decrease of Q_1 with aging can therefore be interpreted as a

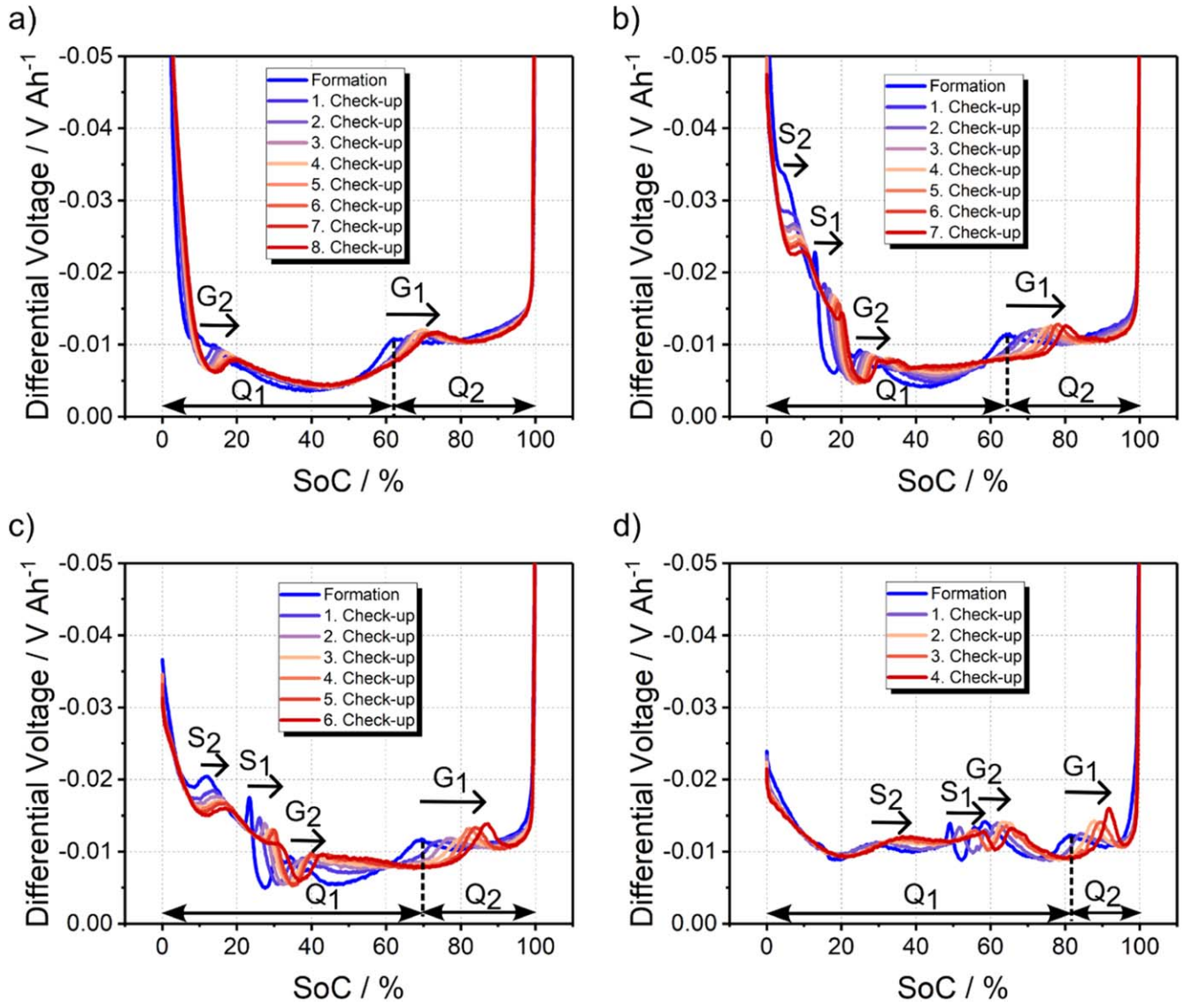

Figure 5. Comparative plot of DVA for one cell each calendar aged at 45 °C/100% SoC of (a) graphite, (b) SiG3.0, (c) SiG5.8, and (d) SiG20.8 for the discharge curves of the last formation cycle and the check-ups performed. The capacities are normalized to SoC = 100%. The arrows indicate the shift in Si peaks S_1 and S_2 and graphite peaks G_1 and G_2 due to calendar aging. The central graphite peak G_1 from the formation is highlighted by a dashed vertical line for each cell type and divides the capacity into two characteristic portions Q_1 and Q_2. These allow assignment of the calendar aging contributions into a LAAM (change Q_1) and a LLI (change Q_2).[50,51]

degradation of the anode, i.e. LAAM. The capacity fraction Q_2 is calculated from the distance between the graphite peak G_1 and 100% SoC. It contains information about the electrode balancing.[50,51] Absolute changes of Q_2 during aging without simultaneous changes of the anode and cathode capacities can be interpreted as LLI.[50,51] Figure 6 plots the Q_1 and Q_2 values calculated from the DVAs for the cells aged at 45 °C and 100% SoC, taking into account their actual SoHs. For each cell type, the corresponding ratio of the capacity fractions from the formation is compared with that from the last check-up performed in this study (Graphite) or before reaching the EoL criterion (SiG3.0, SiG5.8 and SiG20.8).

When comparing the Q_1 values of the aged cells with the respective reference values from the formation, differences can be observed between the pure graphite and the Si-containing cells. For the former, there is no evidence indicating degradation of the anode. Therefore, the overall decrease in capacity is attributed to the decrease of the Q_2 value and thus solely to LLI and not to a change in balancing (N/P ratio). The LLI is assumed to result from reductive decomposition of the electrolyte and the associated SEI growth, as explained above. In the presence of Si, however, not only the Q_2 value but also the fraction of the anode storage capability Q_1 decreases due to calendar aging, so that for the Si based cells an additional LAAM can be assumed with respect to the Si component. The reduction of the capacity fraction Q_1 increases with increasing Si content and is greatest for SiG20.8. Nevertheless, the dominant part of the capacity loss is due to the decrease in the Q_2 fraction for these cells. Thus, for the Si-containing cells, the mechanism of the calendar aging seems to consist mainly of LLI and complementary of LAAM which increases with increasing Si content.

Post-Mortem analysis.—In Fig. 7, SEM top views of graphite and SiG5.8 anode surfaces are compared exemplarily. After formation, the graphite particles in the pure graphite anode (Fig. 7a) have relatively smooth surfaces and clear edges. In contrast, the visible surfaces of the anode aged at 45 °C and 100% SoC (Fig. 7b) show a higher roughness. EDX-mappings of the unaged anode indicate no presence of either Fluorine or Phosphorous. In contrast, a Fluorine content of ∼3.4 wt−% and a Phosphorous content of ∼0.7 wt−% were detected in the electrode after calendar aging. Since Fluorine and Phosphorous are typical building blocks of the SEI layer formed on graphite

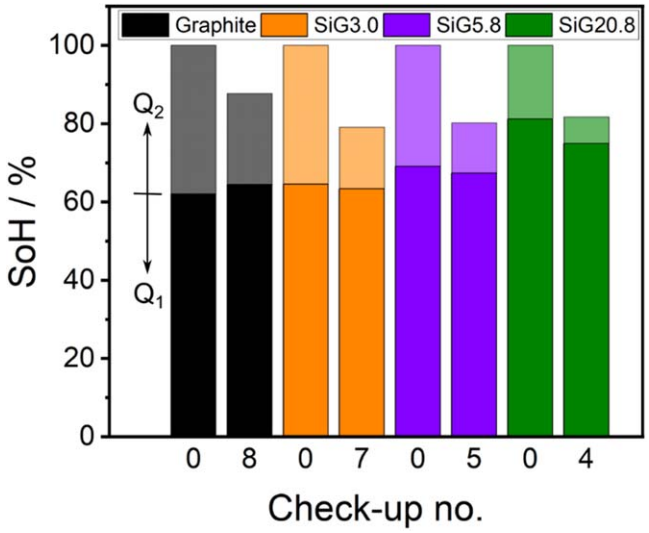

Figure 6. Evaluation of Q_1 and Q_2 from DVA. Each column corresponds to the average of two cells.

particles,[16,31] it can be assumed that the structures visible on the surface of the graphite particles in the SEM image are most likely electrolyte decomposition products as part of the SEI. This is consistent with the indications based on the electrochemical analysis suggesting SEI growth with LLI aging mechanism for the pure graphite anodes.

The SiG5.8 anode (Fig. 7c) is also characterized by smooth graphite particles after formation. In contrast to the pure graphite anode, there is no film formation observable on the surfaces of the graphite particles of the calendar aged SiG5.8 anode (Fig. 7d). However, we note that this might be due to the different electrolyte additives for graphite (VC) and Si/graphite (FEC). The SEI growth in the Si/graphite cells suggested by the electrochemical data therefore probably mainly affects the Si component.

In order to better characterize the Si particles, SEM images of electrode cross-sections were carried out. The corresponding sections of a representative particle of the SiG5.8 anodes after formation and after calendar aging (45 °C and 100% SoC) are compared in Fig. 8. It is important to note that the visible μm-scaled Si compounds are themselves composed of nm-scaled Si particles. The Si particles are embedded in a carbon matrix with a carbon coating surrounding the entire μm-sized structure (see e.g. film of darker grey indicated in Fig. 8d). While the nm-size of the Si particles decreases the diffusion paths of Li in Si,[58] the observed

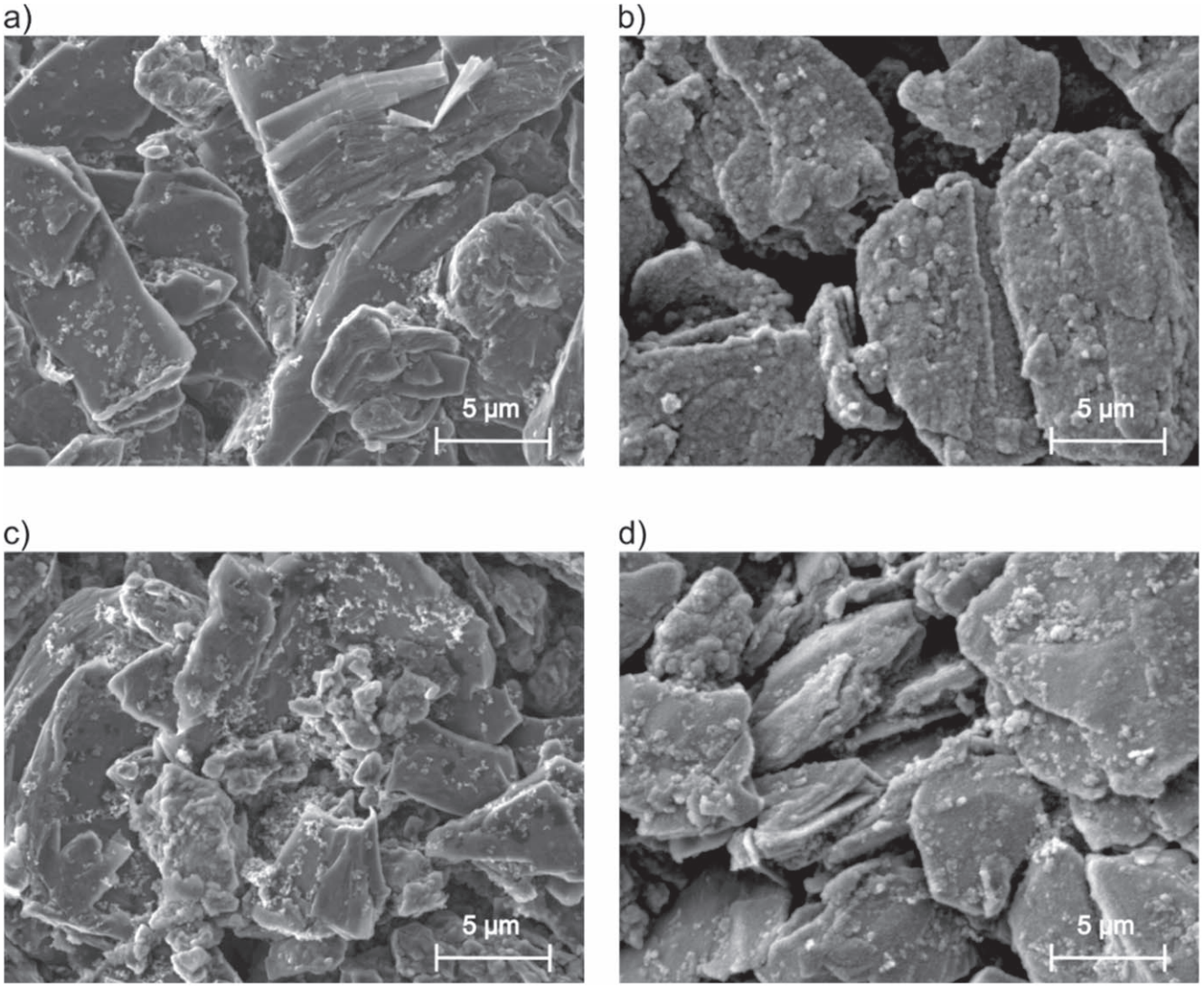

Figure 7. SEM measurements of anodes from (a)-(b) graphite based and (c)-(d) SiG5.8 based cells at 5000x magnification. Anodes a) and c) are from cells after formation and anodes (b) and (d) are from calendar aged cells at 45 °C/100% SoC.

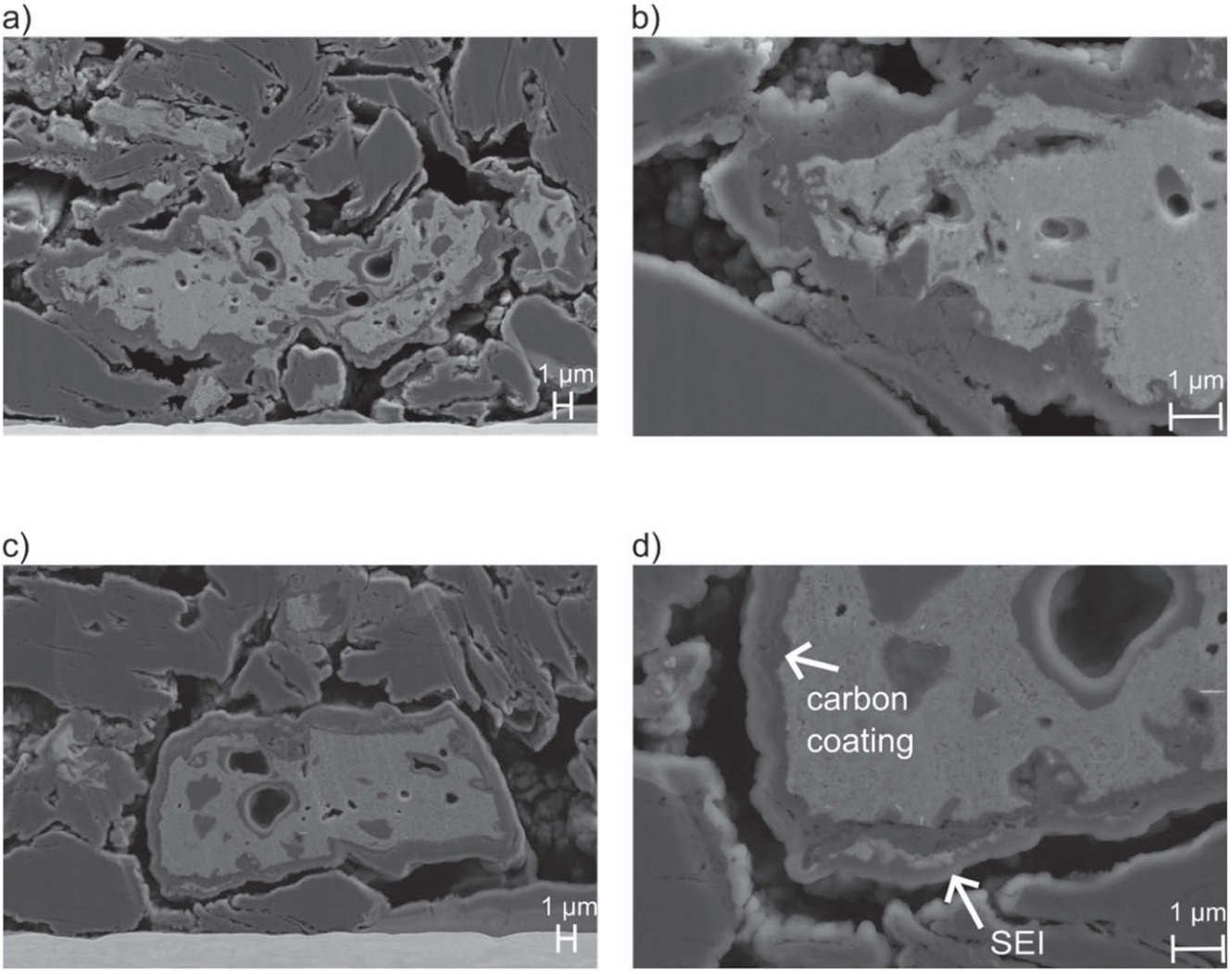

Figure 8. Comparative SEM cross-sections of representative Si particles of SiG5.8 anodes from a cell (a)-(b) after formation and (c)-(d) after calendar aging at 45 °C and the storage SoC of 100%. Images (a) and (c) were recorded at 10000x magnification and images (b) and (d) at 30000x magnification. The arrows in (d) indicate the intrinsic carbon coating and the SEI layer.

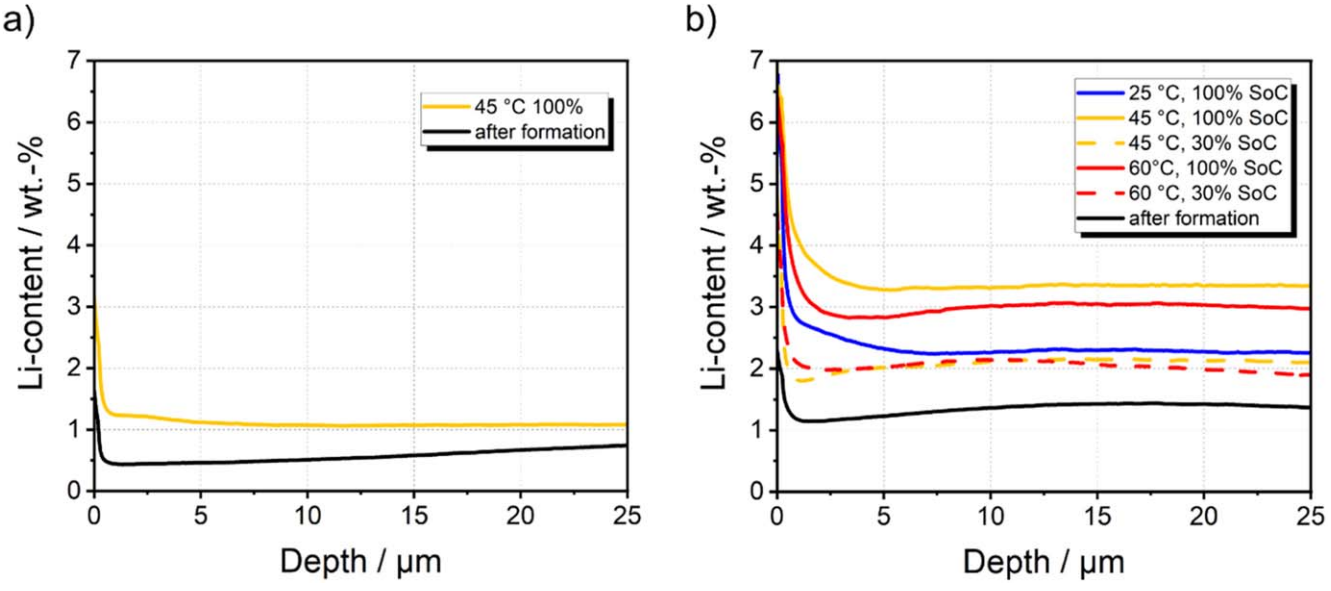

Figure 9. Comparative plot of the GD-OES depth profile of the Li content of anodes from (a) graphite based and (b) SiG5.8 based cells.

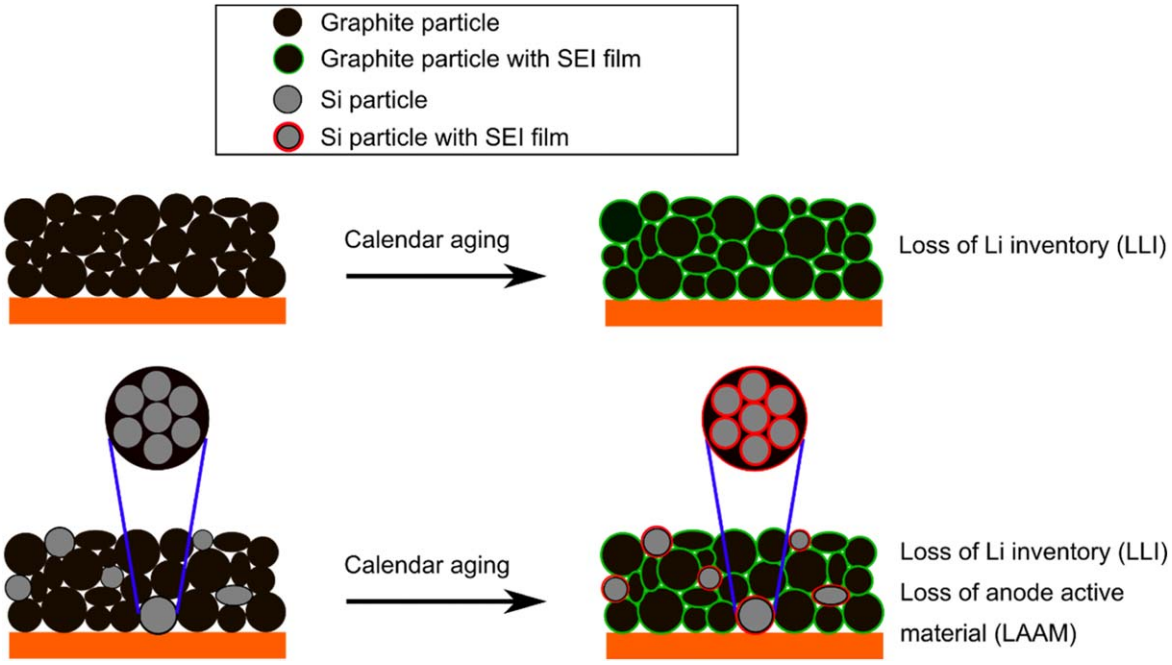

Figure 10. Schematic representation of the calendar aging mechanism in the pure graphite cells (top) and the Si/graphite cells (bottom).

Table III. Summary of the calendar aging behavior of cells with graphite and Si/graphite anodes.

Graphite		Si/graphite
	square-root decrease of capacity with time faster aging with higher temperature (Arrhenius-like) fastest aging at highest SoC of 100%	
aging of pure graphite slower than with Si SEI growth on graphite –> LLI		faster aging with higher Si content SEI growth on graphite –> LLI SEI growth on Si –> LLI + LAAM

particle composite architecture is commonly used to minimize the volume expansion of Si particles during lithiation[9] and was also found in commercial cells.[8]

In addition to the intrinsic carbon coating of the μm-sized Si/carbon particles, the surface of these particles appears to be covered by another very thin film after formation (film of lighter grey in Figs. 8a–8b), which is most likely a SEI layer formed during formation. After calendar aging, the additional surface film around the Si/carbon secondary microparticle (film of lighter grey in Figs. 8c–8d) is still very thin compared to our earlier observation with commercial cells (cell type C in Ref. 8). Thus, no significant aging-induced SEI growth can be observed for the μm-scaled composite as a whole. In contrast, the SEI formation suggested by the electrochemical analysis most likely takes place on the surfaces of the embedded nano-sized primary Si particles. However, this cannot be observed by SEM due to resolution limitations. In the literature it is reported, that Li- and O-rich SEI components form especially on Si particles.[59,60] According to Philippe et al.,[59] such components are Li silicates with the general formula of $Li_xSi_yO_z$, which were also found by Richter et al.[11] for Si/graphite anodes in commercial cells. Therefore, it is conceivable that such species might also be formed during calendar aging with the active material used in this study, thereby consuming both cyclable Li^+-ions and the Si active material itself. This leads to the suggested combination of LLI and LAAM as the main aging mechanism for the Si-containing cells.

The Li contents in graphite and SiG5.8 anodes were quantified by GD-OES depth profiling. When comparing the unaged and calendar aged anodes in Fig. 9 it can be noted that the Li content is lower both at the surface and in the bulk material for the unaged cells. The increase in Li content in the electrodes due to calendar aging can be taken as an indication of an irreversible loss of cyclable Li^+-ions in favor of the growth of the SEI layer.

For the SiG5.8 anodes calendar aged at 45 °C and 60 °C (Fig. 9b) a higher amount of Li was determined in the corresponding anodes for the cells aged at 100% SoC compared to their analogues aged at 30% SoC. This finding correlates well with the highest capacity losses found for the highest SoC studied. Moreover, the quantified Li contents in the Si-containing anodes are higher than in the graphite based counterparts. Accordingly, the presence of Si seems to enhance irreversible Li accumulation in the anode, which could explain the higher irreversible capacity losses of the Si/graphite cells compared to the graphite-only cells.

Table III summarizes all characteristics of the calendar aging behavior found for the investigated cell types. These indications suggest a different main aging mechanism for the Si/graphite anodes in comparison to the pure graphite anodes. As shown schematically in Fig. 10, calendar aging results from SEI growth in both cases, but leads to pure LLI for the graphite anodes, while it additionally consumes the Si active material itself in the Si/graphite cells, leading to LLI and LAAM as the main aging mechanism.

Conclusions

In this detailed study with 121 Li-ion pouch full cells containing pure graphite as well as Si/graphite anodes, the main mechanisms for calendar aging were investigated. The following results on cell level can be reported:

- Capacity fade follows a square-root function with time for all cell types. The aging rate changes with time and can be described by the derivation of the square-root function.
- The aging rate increases with temperature following an Arrhenius-like behavior. Time-dependent 3D Arrhenius plots show the highest aging rates in the beginning of aging and an attenuation with aging time.
- The highest capacity losses were found after aging at 100% SoC followed by 60% SoC and 30% SoC.
- In general, a faster capacity decrease was identified for the Si/graphite cells compared to the pure graphite cells. With respect to the Si content a clear trend of increasing aging rates with increasing Si content was observed. However, this trend is not in the same direction for all aging conditions studied.

Post-Mortem analysis revealed the following trends on electrode level:

- An aging-induced film growth is detectable by SEM on the surface of the pure graphite anodes, however, not for the Si/graphite anodes. In this context, the structure of the Si/carbon secondary microparticles should be emphasized, which contain embedded nano-Si particles. The SEI growth occurs most likely on the surfaces of the Si nanoparticles, which is not visible by SEM.
- GD-OES depth profiling revealed an increased Li content for anodes from calendar aged cells compared to fresh cells. With increasing SoC, higher amounts of Li were detected in Si-containing anodes. Overall, the quantified Li contents are higher in aged cells with Si component compared to pure graphite anodes.

It can be concluded, that the main aging mechanism for the investigated cells containing graphite or Si/graphite anodes most likely is SEI growth, with the SEI irreversibly binding Li in the anode. In case of graphite anodes, SEI growth happens on the surface of the graphite particles only, leading only to LLI. Since SEI is a surface modification of graphite particles only and no bulk modification, LAAM does not play a significant role for graphite anodes.

In contrast, for Si/graphite anodes investigated in this paper, SEI growth leads to both LLI and LAAM. In case of the Si compound, SEI growth affects also the Si active material itself, leading not only to LLI as for graphite. The cause for such different behavior is still to be investigated and most likely will be also subject to the Si properties in the anode. This point is important since LAAM can change the N/P ratio and therefore influence the susceptibility to Li plating. Therefore, the mechanism in calendar aging is relevant for the safety in second-life applications. Further investigations on this direction are ongoing in our labs.

Acknowledgments

Funding of the projects CharLiSiKo (03XP0333A) and MiCha (03XP0317C) in the AQua-Cluster by the German Federal Ministry of Education and Research (BMBF) and project management by Projektträger Jülich (PtJ) are gratefully acknowledged. All investigations in this work were carried out at ZSW. The authors would like to thank A. Aracil Regalado and C. Pfeifer (ZSW) for SEM/EDX measurements and Prof. A. Latz (HIU, DLR) for fruitful discussions.

ORCID

Katharina Bischof https://orcid.org/0009-0004-0321-3252
Marius Flügel https://orcid.org/0000-0002-9792-0414
Margret Wohlfahrt-Mehrens https://orcid.org/0000-0002-5118-5215
Thomas Waldmann https://orcid.org/0000-0003-3761-1668

References

1. M. Dubarry, N. Qin, and P. Brooker, *Current Opinion in Electrochemistry*, **9**, 106 (2018).
2. C. Wang, C. Yang, and Z. Zheng, *Advanced Science*, **9**, 2105213 (2022).
3. F. Ozanam and M. Rosso, *Materials Science and Engineering: B*, **213**, 2 (2016).
4. F. Luo, B. Liu, J. Zheng, G. Chu, K. Zhong, H. Li, X. Huang, and L. Chen, *J. Electrochem. Soc.*, **162**, A2509 (2015).
5. J. D. McBrayer et al., *Nat. Energy*, **6**, 866 (2021).
6. X. Zuo, J. Zhu, P. Müller-Buschbaum, and Y.-J. Cheng, *Nano Energy*, **31**, 113 (2017).
7. M. Armand et al., *J. Power Sources*, **479**, 228708 (2020).
8. M. Flügel, K. Richter, M. Wohlfahrt-Mehrens, and T. Waldmann, *J. Electrochem. Soc.*, **169**, 50533 (2022).
9. F. Dou, L. Shi, G. Chen, and D. Zhang, *Electrochemical Energy Reviews*, **2**, 149 (2019).
10. M. Schindler, J. Sturm, S. Ludwig, A. Durdel, and A. Jossen, *J. Electrochem. Soc.*, **168**, 60522 (2021).
11. K. Richter, T. Waldmann, M. Kasper, C. Pfeifer, M. Memm, P. Axmann, and M. Wohlfahrt-Mehrens, *J. Phys. Chem.*, C**123**, 18795 (2019).
12. J. Schmitt, M. Schindler, and A. Jossen, *J. Power Sources*, **506**, 230240 (2021).
13. D. Anseán, G. Baure, M. González, I. Cameán, A. B. García, and M. Dubarry, *J. Power Sources*, **459**, 227882 (2020).
14. X. Li, A. M. Colclasure, D. P. Finegan, D. Ren, Y. Shi, X. Feng, L. Cao, Y. Yang, and K. Smith, *Electrochim. Acta*, **297**, 1109 (2019).
15. K. Kalaga, M.-T. F. Rodrigues, S. E. Trask, I. A. Shkrob, and D. P. Abraham, *Electrochim. Acta*, **280**, 221 (2018).
16. T. Waldmann, M. Wilka, M. Kasper, M. Fleischhammer, and M. Wohlfahrt-Mehrens, *J. Power Sources*, **262**, 129 (2014).
17. J. Vetter, P. Novák, M. R. Wagner, C. Veit, K.-C. Möller, J. O. Besenhard, M. Winter, M. Wohlfahrt-Mehrens, C. Vogler, and A. Hammouche, *J. Power Sources*, **147**, 269 (2005).
18. L. Y. Beaulieu, T. D. Hatchard, A. Bonakdarpour, M. D. Fleischauer, and J. R. Dahn, *J. Electrochem. Soc.*, **150**, A1457 (2003).
19. I. Zilberman, J. Sturm, and A. Jossen, *J. Power Sources*, **425**, 217 (2019).
20. L. de Sutter, G. Berckmans, M. Marinaro, J. Smekens, Y. Firouz, M. Wohlfahrt-Mehrens, J. van Mierlo, and N. Omar, *Energies*, **11**, 2948 (2018).
21. W. Lu, L. Zhang, Y. Qin, and A. Jansen, *J. Electrochem. Soc.*, **165**, A2179 (2018).
22. M. Flügel, M. Bolsinger, M. Marinaro, V. Knoblauch, M. Hölzle, M. Wohlfahrt-Mehrens, and T. Waldmann, *J. Electrochem. Soc.*, **170**, 60536 (2023).
23. D. Aurbach, K. Gamolsky, B. Markovsky, Y. Gofer, M. Schmidt, and U. Heider, *Electrochim. Acta*, **47**, 1423 (2002).
24. J. C. Burns, R. Petibon, K. J. Nelson, N. N. Sinha, A. Kassam, B. M. Way, and J. R. Dahn, *J. Electrochem. Soc.*, **160**, A1668 (2013).
25. I. A. Shkrob, J. F. Wishart, and D. P. Abraham, *The Journal of Physical Chemistry C*, **119**, 14954 (2015).
26. C. Xu, F. Lindgren, B. Philippe, M. Gorgoi, F. Björefors, K. Edström, and T. Gustafsson, *Chem. Mater.*, **27**, 2591 (2015).
27. M. Ecker, J. B. Gerschler, J. Vogel, S. Käbitz, F. Hust, P. Dechent, and D. U. Sauer, *J. Power Sources*, **215**, 248 (2012).
28. J. Schmitt, A. Maheshwari, M. Heck, S. Lux, and M. Vetter, *J. Power Sources*, **353**, 183 (2017).
29. J. Schmalstieg, S. Käbitz, M. Ecker, and D. U. Sauer, *J. Power Sources*, **257**, 325 (2014).
30. S. Käbitz, J. B. Gerschler, M. Ecker, Y. Yurdagel, B. Emmermacher, D. André, T. Mitsch, and D. U. Sauer, *J. Power Sources*, **239**, 572 (2013).
31. E. Peled, *J. Electrochem. Soc.*, **126**, 2047 (1979).
32. H. J. Ploehn, P. Ramadass, and R. E. White, *J. Electrochem. Soc.*, **151**, A456 (2004).
33. M. Broussely, S. Herreyre, P. Biensan, P. Kasztejna, K. Nechev, and R. Staniewicz, *J. Power Sources*, **97-98**, 13 (2001).
34. F. Single, A. Latz, and B. Horstmann, *ChemSusChem*, **11**, 1950 (2018).
35. M. B. Pinson and M. Z. Bazant, *J. Electrochem. Soc.*, **160**, A243 (2013).
36. J. Christensen and J. Newman, *J. Electrochem. Soc.*, **151**, A1977 (2004).
37. F. Single, B. Horstmann, and A. Latz, *J. Electrochem. Soc.*, **164**, E3132 (2017).
38. S. Shi, P. Lu, Z. Liu, Y. Qi, L. G. Hector, H. Li, and S. J. Harris, *J. Am. Chem. Soc.*, **134**, 15476 (2012).
39. C. R. Birkl, M. R. Roberts, E. McTurk, P. G. Bruce, and D. A. Howey, *J. Power Sources*, **341**, 373 (2017).
40. X. Han, L. Lu, Y. Zheng, X. Feng, Z. Li, J. Li, and M. Ouyang, *eTransportation*, **1**, 100005 (2019).
41. G. Kucinskis, M. Bozorgchenani, M. Feinauer, M. Kasper, M. Wohlfahrt-Mehrens, and T. Waldmann, *J. Power Sources*, **549**, 232129 (2022).
42. P. Atkins, J. De Paula, and J. Keeler, *Atkins' Physical Chemistry* (Oxford University Press, Oxford) (2023).
43. T. Waldmann, M. Kasper, and M. Wohlfahrt-Mehrens, *Electrochim. Acta*, **178**, 525 (2015).
44. X.-G. Yang and C.-Y. Wang, *J. Power Sources*, **402**, 489 (2018).
45. M. Feinauer, A. A. Abd-El-Latif, P. Sichler, A. Aracil Regalado, M. Wohlfahrt-Mehrens, and T. Waldmann, *J. Power Sources*, **570**, 233046 (2023).

46. M. Bozorgchenani, G. Kucinskis, M. Wohlfahrt-Mehrens, and T. Waldmann, *J. Electrochem. Soc.*, **169**, 30509 (2022).
47. T. Waldmann, N. Ghanbari, M. Kasper, and M. Wohlfahrt-Mehrens, *J. Electrochem. Soc.*, **162**, A1500 (2015).
48. B. Y. Liaw, E. P. Roth, R. G. Jungst, G. Nagasubramanian, H. L. Case, and D. H. Doughty, *J. Power Sources*, **119–121**, 874 (2003).
49. J. Wang, P. Liu, J. Hicks-Garner, E. Sherman, S. Soukiazian, M. Verbrugge, H. Tataria, J. Musser, and P. Finamore, *J. Power Sources*, **196**, 3942 (2011).
50. P. Keil, S. F. Schuster, J. Wilhelm, J. Travi, A. Hauser, R. C. Karl, and A. Jossen, *J. Electrochem. Soc.*, **163**, A1872 (2016).
51. P. Keil and A. Jossen, *J. Electrochem. Soc.*, **164**, A6066 (2017).
52. M. Dubarry, C. Truchot, and B. Y. Liaw, *J. Power Sources*, **219**, 204 (2012).
53. T. Ohzuku, Y. Iwakoshi, and K. Sawai, *J. Electrochem. Soc.*, **140**, 2490 (1993).
54. M. Ashuri, Q. He, and L. L. Shaw, *Nanoscale*, **8**, 74 (2016).
55. V. G. Khomenko, V. Z. Barsukov, J. E. Doninger, and I. V. Barsukov, *J. Power Sources*, **165**, 598 (2007).
56. R. Jung, M. Metzger, F. Maglia, C. Stinner, and H. A. Gasteiger, *J. Electrochem. Soc.*, **164**, A1361 (2017).
57. H.-J. Noh, S. Youn, C. S. Yoon, and Y.-K. Sun, *J. Power Sources*, **233**, 121 (2013).
58. M. Weiss et al., *Adv. Energy Mater.*, **11**, 2101126 (2021).
59. B. Philippe, R. Dedryvère, M. Gorgoi, H. Rensmo, D. Gonbeau, and K. Edström, *Chem. Mater.*, **25**, 394 (2013).
60. B. Philippe, R. Dedryvère, J. Allouche, F. Lindgren, M. Gorgoi, H. Rensmo, D. Gonbeau, and K. Edström, *Chem. Mater.*, **24**, 1107 (2012).